



HAL
open science

Synthesis and transport properties of the Te-substituted homologous compounds $\text{Pb}_5\text{Bi}_6\text{Se}_{14-x}\text{Te}_x$ ($0 \leq x \leq 1.0$)

Selma Sassi, Christophe Candolfi, Christine Gendarme, Anne Dauscher,
Bertrand Lenoir

► To cite this version:

Selma Sassi, Christophe Candolfi, Christine Gendarme, Anne Dauscher, Bertrand Lenoir. Synthesis and transport properties of the Te-substituted homologous compounds $\text{Pb}_5\text{Bi}_6\text{Se}_{14-x}\text{Te}_x$ ($0 \leq x \leq 1.0$). Dalton Transactions, 2018, 47 (13), pp.4714-4721. 10.1039/c7dt04916a . hal-02391405

HAL Id: hal-02391405

<https://hal.science/hal-02391405>

Submitted on 24 Mar 2020

HAL is a multi-disciplinary open access archive for the deposit and dissemination of scientific research documents, whether they are published or not. The documents may come from teaching and research institutions in France or abroad, or from public or private research centers.

L'archive ouverte pluridisciplinaire **HAL**, est destinée au dépôt et à la diffusion de documents scientifiques de niveau recherche, publiés ou non, émanant des établissements d'enseignement et de recherche français ou étrangers, des laboratoires publics ou privés.

Synthesis and transport properties of the Te-substituted homologous compounds



Selma Sassi, Christophe Candolfi, Christine Gendarme, Anne Dauscher and Bertrand Lenoir*

Institut Jean Lamour, UMR 7198 CNRS – Université de Lorraine, 2 allée André Guinier-

Campus ARTEM, BP 50840, 54011 Nancy Cedex, France

*Corresponding author: bertrand.lenoir@univ-lorraine.fr

Abstract

The crystal structure and transport properties (2 – 723 K) of the homologous compound $\text{Pb}_5\text{Bi}_6\text{Se}_{14}$ with partial substitution of Te for Se are studied by means of powder X-ray diffraction, scanning electron microscopy, electrical resistivity, thermopower, thermal conductivity and Hall effect measurements. Polycrystalline samples $\text{Pb}_5\text{Bi}_6\text{Se}_{14-x}\text{Te}_x$ ($0 \leq x \leq 1.0$) were prepared by a two-step synthesis method based on the pseudo-binary PbSe-Bi₂Se₃ phase diagram combined with Te substitution in the PbSe precursor. The successful insertion of Te into the crystal structure of $\text{Pb}_5\text{Bi}_6\text{Se}_{14}$ was confirmed by powder X-ray diffraction and scanning electron microscopy. Transport properties measurements indicate an increase in the heavily-doped character of the transport with increasing the Te concentration. The extremely low lattice thermal conductivity values (0.3 – 0.4 W m⁻¹ K⁻¹ at 723 K) that approach the glassy limit at high temperatures are nearly independent of the chemical composition suggesting no influence on point-defect scattering mechanisms in the substituted compounds. Despite the inherent complexity of this system, the evolution of the electronic properties with

x are well described by a simple single-parabolic band model. Because the increase in the power factor with increasing x is compensated by the concomitant increase in the electronic thermal conductivity, this substitution does not yield enhanced ZT values with respect to the pristine compound with similar peak ZT values of 0.5 achieved at 723 K. Nevertheless, the simple synthetic method used in this study to insert a doping element opens new avenues for controlling the transport properties of the homologous series $(\text{PbSe})_5(\text{Bi}_2\text{Se}_3)_{3m}$ ($m = 1, 2$ and 3).

Introduction

Thermoelectricity provides a clean and reliable alternative technology to generate electrical power from various waste heat sources.¹⁻³ Significant efforts were devoted over the last decades to search for novel materials, the thermoelectric properties of which could surpass those of the conventional materials currently used in generators and Peltier coolers. A good thermoelectric material should exhibit a combination of three antagonistic properties, that is, large thermopower α , low electrical resistivity ρ and low thermal conductivity κ to maximize the dimensionless thermoelectric figure of merit $ZT = \alpha^2 T / \rho \kappa$ at a given absolute temperature T .^{1,2} The best compromise between these three seemingly incompatible physical properties is usually achieved in heavily-doped semiconductors crystallizing in complex crystal structures to optimize the power factor α^2 / ρ while trying to maintain the electronic (κ_e) and lattice (κ_L) contributions to the thermal conductivity ($\kappa = \kappa_e + \kappa_L$) as low as possible.¹⁻³

Homologous compounds meet several requirements that can potentially lead to good thermoelectric performances.^{4,5} The complexity of their crystal structure can be manipulated by varying the number of building blocks by regular increments offering an interesting

playground to achieve glass-like lattice thermal conductivity.^{4,5} Their chemical flexibility provides another advantage to modulate the carrier concentration through substitutions or insertion of various elements in channels or between the layers of the crystal structure. Examples of series where promising thermoelectric performances were achieved include the series of pavonite $M_{n+1}\text{Bi}_2\text{S}_{n+5}$ ($M = \text{Ag}/\text{Bi}$ or Cu/Bi and $n \geq 2$) or lillianite $\text{Pb}_{n-1}\text{Bi}_2\text{S}_{n+2}$ (with n being either integer or non-integer) with, so far, a maximum ZT value of 0.9 at 775 K obtained in the ternary lillianite $\text{Pb}_7\text{Bi}_4\text{Se}_{13}$ ($n = 4.5$).⁶⁻⁹

The series $(\text{PbSe})_5(\text{Bi}_2\text{Se}_3)_{3m}$ ($m = 1, 2, 3$ and 4) is a sub-series of the cannizzarites minerals¹⁰⁻¹⁶ and constitute another homologous series of compounds recently studied for their interesting transport properties and for the topologically non-trivial electronic band structure evidenced in the $m = 2$ compound by angle-resolved photoemission spectroscopy.¹⁷⁻²⁸ With no exception, all these compounds crystallize in a monoclinic structure described in the space groups $P2_1/m$ ($m = 1$ and 3), $C2/m$ ($m = 2$) or $P2/m$ ($m = 4$).^{22-24,27,28} Their crystal structure is formed by Pb-Se layers sandwiched by m Bi-Se layers (Figure 1). Transport properties measurements performed on polycrystalline samples showed that all these compounds exhibit n -type behaviour, the nature of which has been tentatively attributed to mixed occupation of Pb and Bi on several sites of the crystal structure.^{22-24,28} While the $m = 1$ compound exhibits semiconducting-like electrical properties, increasing m to 2 and 3 results in nearly similar metallic-like properties.^{25,26,28} As expected from their large, complex unit cell, these compounds display very low lattice thermal conductivity that approaches the glassy limit at high temperatures (between 0.3 and 0.4 $\text{W m}^{-1} \text{K}^{-1}$ at 723 K).^{25,26,28} Remarkably, the way the lattice thermal conductivity evolves with m appears to be unusual with an increase in the κ_L values on going from $m = 1$ to $m = 3$.²⁸ This behaviour contrasts with the general and simple expectation of a decrease in κ_L with increasing the structural complexity, which points to an important role played by the interlayer interfaces on the thermal transport. So far, maximum

ZT values of 0.50, 0.25 and 0.20 at 723 K have been achieved in the $m = 1, 2$ and 3 compounds, respectively.^{25,26,28} Because only pristine samples were investigated, further enhancement in their ZT values may be expected by tuning the electron concentration through substitutions.

Here, the successful synthesis of polycrystalline $\text{Pb}_5\text{Bi}_6\text{Se}_{14-x}\text{Te}_x$ in the substitution range $0 \leq x \leq 1.0$ is reported. The two-step synthesis method used to prepare the ternary compounds can be extended to dope $\text{Pb}_5\text{Bi}_6\text{Se}_{14}$ ($m = 1$) using substituted precursors. In order to drive this semiconducting-like compound towards a heavily-doped state, Te was chosen as the substituting element based on the general observation of an increase in the metallic character of transport in chalcogenides on going from sulfides to tellurides.²⁹⁻³² The successful insertion of Te into the crystal structure is demonstrated by powder X-ray diffraction and scanning electron microscopy. Measurements of the physical properties confirmed our expectations and evidenced a progressive increase in the electron concentration with increasing x . Additionally, despite the probably complex electronic band structure of this compound, the evolution of the electronic properties with x follows a single-parabolic band behaviour.

Experimental section

Synthesis

In prior studies, phase-pure polycrystalline samples of the $m = 1, 2$ and 3 compounds were successfully synthesized by a two-step method following the pseudo-binary phase diagram $\text{PbSe-Bi}_2\text{Se}_3$.^{22-26,28} The present series of polycrystalline Te-substituted compounds was prepared similarly. All the manipulations were carried out in a dry, argon-filled glove box. In

a first step, the two precursors $\text{PbSe}_{1-y}\text{Te}_y$ ($y = 0.05, 0.1$ and 0.2) and Bi_2Se_3 were prepared by loading high-purity powders (Pb, 99.999%; Se, 99.999%; Te, 99.999%; Bi, 99.999%) into evacuated silica glass tubes. The ampules, sealed under secondary vacuum, were heated to 1393 K, held at this temperature for 12 h and cooled to room temperature over 2 h. The two ingots were ground into fine powders. On the basis of laboratory powder X-ray diffraction performed prior to use, all the precursors were phase pure. The powders were then mixed in stoichiometric quantities to obtain the targeted compositions $\text{Pb}_5\text{Bi}_6\text{Se}_{14-x}\text{Te}_x$ with $0 \leq x \leq 1.0$. The mixed powders were cold pressed into cylindrical pellets which were sealed in silica glass tubes under vacuum and annealed at 873 K for ten days. The annealed pellets were again ground into micron-sized powders that were consolidated in a 10-mm-diameter graphite die by spark plasma sintering at 673 K for 10 minutes under a pressure of 80 MPa. The densities of all samples, determined from weight and dimensions, were above 97% of the theoretical density from single-crystal X-ray diffraction data.

Structural and chemical characterizations

Phase purity of the samples was verified by powder X-ray diffraction (PXRD) at 300 K using a Bruker D8 Advance diffractometer ($\text{CuK}\alpha_1$ radiation, $\lambda = 1.54056 \text{ \AA}$). The chemical homogeneity of the samples was probed by scanning electron microscopy (SEM) using a Quanta FEG 650 (FEI) in backscattered electron mode (BSE) in order to contrast possible impurity phases from the main phase. The spatial distribution of the elements was determined by elemental X-ray mapping.

The chemical compositions of the samples were determined by wavelength dispersive X-ray spectroscopy (WDXS) using a JEOL J7600F instrument. PbSe , Bi_2Se_3 , SnSe and PbTe were used as standards to measure the Pb, Bi, Se and Te concentrations, respectively. The

actual chemical compositions were obtained by averaging a minimum of 80 different spots measured on the surface of each samples. All the actual compositions, listed in Table 1, were normalized to 25 atoms per chemical formula. Hereafter, the samples will be labelled by their actual Te content.

Transport properties measurements

Bar-shaped samples with typical dimensions of $2.5 \times 2.5 \times 8$ mm³ were cut with a diamond-wire saw from the consolidated pellets. These samples were cut both perpendicular and parallel to the pressing direction due to the anisotropic crystal structure of these compounds. Low-temperature measurements (5 – 300 K) of the thermopower, electrical resistivity and thermal conductivity were realized simultaneously using the thermal transport option (TTO) of a physical property measurement system (PPMS, Quantum Design). Four copper leads were attached onto the sample using an Ag-containing epoxy (Epotek H20E) to make the electrical and thermal contacts. Owing to thermal radiations that inevitably accompany the measurements of the thermal conductivity below 300 K, the data between 200 and 300 K were discarded.

Measurements of the Hall coefficient R_H were carried out between 5 and 300 K using a five-probe method and the ac transport option of the PPMS. For these measurements, five copper wires were attached onto the samples with a small amount of silver paste. The transverse electrical resistivity ρ_{xy} was measured by sweeping the magnetic field $\mu_0 H$ between -1 and +1 T. The Hall resistivity ρ_H was then determined following the relation $\rho_H = [\rho_{xy}(\mu_0 H) - \rho_{xy}(-\mu_0 H)] / 2$ to dismiss possible magnetoresistive contribution. These measurements were performed on samples cut in both directions to determine the anisotropy in R_H . The Hall carrier concentrations n and Hall mobilities μ_H were determined within a

single-carrier picture by the formulas $R_H = 1/ne$ where e is the elementary charge and $\mu_H = R_H/\rho$. Noteworthy, in anisotropic crystals, the galvanomagnetic properties are described by a tensor with several independent components, the number of which depends on the symmetry of the crystal.³³ The R_H values measured in polycrystalline samples correspond to a mixing of these different components. In principle, in the case of strongly anisotropic R_H values, the above-mentioned simple formulas relating n and μ_H to R_H cannot be used. However, the anisotropy in the present series of samples remains moderate and evolves neither with temperature nor with x , which justifies the approximation used herein.²⁸ The modelling of the transport data was carried out by taking the values of the electron concentrations and Hall mobilities measured in the perpendicular direction. The main conclusions drawn from this model would not be affected by considering the values measured in the parallel direction.

Thermopower and electrical resistivity were measured simultaneously between 300 and 723 K with a ZEM-3 system (Ulvac-Riko) on bar-shaped samples of similar dimensions. The thermal conductivity κ was determined in the same temperature range by measuring the thermal diffusivity a by a laser flash technique (LFA 427, Netzsch). The thermal conductivity was then calculated from the relation $\kappa = aC_p d$ where d is the experimental density of the sample. The specific heat was assumed to be equal to the Dulong-Petit value above 300 K while the temperature dependence of the density has been neglected. The combined experimental uncertainty in ZT above 300 K is estimated to be 17%.³⁴

Results and discussion

Structural and chemical characterizations

Our two-step synthesis procedure successfully yields Te-substituted samples with the targeted compositions as shown by a comparison of the experimental PXRD pattern with the theoretical pattern calculated using single-crystal structure data (Figure 2). In addition to the overall good matching of peak positions between the experimental and theoretical patterns, these measurements do not evidence the presence of any secondary phases within the experimental error of this technique. However, the strongly anisotropic crystal structure of these compounds results in a preferred orientation of the crystallites of the powder which significantly modifies the relative intensities of the Bragg reflections. In particular, the series of ($h00$) reflections are systematically more intense than expected. This strong preferred orientation did not allow further analyses of these patterns by Rietveld refinements to accurately determine the variations in the lattice parameters with x . The absence of additional reflections in the patterns of the Te-substituted samples further indicate that Te atoms do not show any ordering and thus, are randomly distributed in the crystal structure. Whether Te atoms exhibit preferential occupation on several Se sites cannot be easily determined due to the 14 independent positions of Se atoms in the unit cell of these compounds.

Figure 3 shows a typical SEM image in backscattered electron mode (BSE) and the corresponding X-ray maps collected on the $x = 0.20$ sample. Additional analyses performed on the $x = 0.44$ and 0.95 samples can be found in Figures S1 and S2 in the Electronic Supplementary Information file. For the $x = 0.20$ and 0.44 samples, these analyses indicate an overall good chemical homogeneity reflected by a homogeneous distribution of the four elements in the different samples. When the Te concentration increases to $x = 0.95$, the

elements are less homogeneously distributed than in the other samples (see Table 1 and Figure S2 in the ESI file). In addition, some small Te-rich areas are visible in some of these images suggesting that the actual Te concentrations slightly differ from the nominal contents. This assumption is confirmed by EPMA analyses which show slight under-stoichiometry in the Te contents with respect to the targeted concentrations (see Table 1). While for the $x = 0.20$ and 0.44 samples an overall good match between the actual and nominal compositions is observed, EPMA indicates more significant deviations from the nominal compositions in the $x = 0.95$ sample, especially for the Pb and Bi concentrations. The situation is reminiscent to what has been observed recently in the $m = 2$ and $m = 3$ compounds of this series for which similar deviations were evidenced suggesting that these compounds might be prone to deviations from the ideal stoichiometry.²⁸ As shown below, such deviations do not seem to significantly influence the transport since the data of the $x = 0.95$ sample closely follow the trend predicted from the data of the $x = 0.0, 0.20$ and 0.44 samples.

Electronic transport properties

Figures 4a and 4b show the temperature dependences of the electrical resistivity and thermopower, respectively. The temperature dependence of the $x = 0.0$ sample shows a complex behaviour with two maxima near 200 and 650 K. While the former may be related to changes in the mobility and/or scattering mechanisms of the charge carriers, the high-temperature maximum likely marks the onset of minority carrier activation across the band gap. Both maxima are strongly lessened upon substituting Te for Se in the $x = 0.20$ and 0.44 samples. However, while the low-temperature behaviour is no longer visible for $x = 0.95$, the high-temperature maximum is still discernible in all samples and tends to shift towards higher temperatures with respect to the $x = 0.0$ sample. The fact that the Te-substituted samples

experience minority carrier effects at higher temperatures is consistent with their increased metallic character with increasing x , as demonstrated by the ρ values which decrease with increasing x . Meanwhile, the significant anisotropy between the parallel and perpendicular directions observed in the ternary compound is preserved in the substituted samples but is strongly reduced for $x = 0.95$.

The thermopower data (Figure 4b) confirm this trend with a decrease in the α values (in absolute values) with increasing the Te content from -240 to $-150 \mu\text{V K}^{-1}$ at 723 K in the parallel direction. Above 300 K , a small anisotropy is observed which tends to increase with increasing temperature. Although its magnitude is at the border of the experimental uncertainty of these measurements, the values measured are systematically higher in the parallel direction than in the perpendicular direction, suggesting that this anisotropy is an intrinsic property of these compounds. The anisotropic α values may reflect an asymmetry in the electron-hole density-of-states effective masses due to asymmetric dispersion of the valence and conduction bands. In the $x = 0.0$ sample, the α values tend to level off above 600 K consistent with the hypothesis that this sample experiences minority carrier effects as suggested by the $\rho(T)$ data. From the Goldsmid-Sharp relation $E_g = 2e\alpha_{max}T_{max}$ that relates the band gap E_g to the maximum value α_{max} reached at T_{max} , an E_g value of 0.34 eV is obtained.³⁵ This value is in fair agreement with the value of 0.43 eV inferred from optical absorption spectroscopy.²⁸

The progressive shift towards degenerate semiconducting behaviour with increasing x is reflected by the monotonous decrease in the Hall coefficient R_H (not shown). The negative values are in agreement with the sign of the thermopower confirming that electrons are the majority carriers in these samples. The lack of temperature dependence of the electron concentration n (Figure 5a) for all compounds further confirms that these samples can be classified as degenerate semiconductors. The temperature dependence of the Hall mobility μ_H

(Figure 5b) indicates that neutral impurity scattering dominates below 100 K ($\mu_H \propto cste$) in all compounds. Above this temperature, scattering by acoustic phonons ($\mu_H \propto T^{-3/2}$) starts to play a role which explains the slight decrease in μ_H in the ternary compound. A clearer crossover from neutral impurity to acoustic phonon scattering occurs near 100 K in the Te-containing compounds.

In order to rationalize the evolution of the electronic properties with x , the relationship between n and α has been modelled using solutions to the Boltzmann transport equation within the relaxation time approximation. Assuming a single parabolic band and a single scattering mechanism, the electron concentration and thermopower are given by the following expressions³⁶

$$\alpha = \frac{k_B}{e} \left(\frac{(2 + \lambda)F_{1+\lambda}(\eta)}{(1 + \lambda)F_\lambda(\eta)} - \eta \right) \quad (1)$$

$$n = 4\pi \left(\frac{2m^*k_B T}{h^2} \right)^{\frac{3}{2}} F_{\frac{1}{2}}(\eta) \quad (2)$$

In these relations, k_B is the Boltzmann constant, h is the Planck constant, η is the reduced Fermi energy, m^* is the density-of-states effective mass, λ is the scattering parameter that depends on the dominant scattering mechanism and $F_i(\eta)$ is the Fermi integral defined as

$$F_i(\eta) = \int_0^\infty \frac{\xi^i d\xi}{1 + e^{\xi-\eta}} \quad (3)$$

with ξ the reduced energy of the charge carriers. This single-parabolic band model (SPB) has been applied at 300 and 500 K assuming acoustic phonon scattering ($\lambda = 0$) as the dominant scattering mechanism, as suggested by Hall effect measurements. This analysis has not been

applied at higher temperatures due to the minority carrier effects experienced by the $x = 0.0$ compound above 600 K. This model yields a density-of-states effective mass of $0.52 m_e$ (m_e is the bare electron mass) using the experimental α and n values of the $x = 0.0$ compound. As illustrated in Figure 6, the Ioffe-Pisarenko curves generated at 300 and 500 K by this simple model provides a satisfying description of the electron dependence of the thermopower in the concentration range studied, suggesting that m^* is not significantly affected by the substitution of Te for Se. The fact that a single parameter enables to describe the transport in this concentration range contrasts with the $\text{Pb}_7\text{Bi}_4\text{Se}_{13}$ compound for which a complex electronic band structure with multiple valence band maxima in the vicinity of the Fermi level and anisotropic density-of-states effective masses gives rise to a multiband character of transport.⁸ The difference between both compounds suggests that either a single parabolic valence band or several valence bands with very similar m^* govern the transport in $\text{Pb}_5\text{Bi}_6\text{Se}_{14}$.

Thermal transport properties

The total thermal conductivity as a function of temperature is shown in Figure 7a. For all samples, the anisotropy observed in the electrical resistivity is reversed with the κ values measured in the parallel direction systematically lower than in the perpendicular direction. The main characteristics of the thermal transport of the $x = 0.0$ compound are preserved upon substituting Te for Se, that is, the absence of a low-temperature Umklapp peak and very low values that remain below $1 \text{ W m}^{-1} \text{ K}^{-1}$ in the whole temperature range. The slight increase in κ with increasing x is due to the concomitant increase in the electronic contribution κ_e . To confirm this, κ_e was estimated using the Wiedemann-Franz relation $\kappa_e = LT/\rho$ where L is the

Lorenz number. Temperature-dependent Lorenz numbers were calculated within the SPB model for which L is expressed as³⁶

$$L = \left(\frac{k_B}{e}\right)^2 \left[\frac{(1 + \lambda)(3 + \lambda)F_\lambda(\eta)F_{2+\lambda}(\eta) - (2 + \lambda)^2 F_{1+\lambda}(\eta)^2}{(1 + \lambda)^2 F_\lambda(\eta)^2} \right] \quad (4)$$

As expected, the electronic contribution increases with x for both directions. The lattice thermal conductivity values are very low at 300 K and further decreases with increasing temperature to 0.3 and 0.4 W m⁻¹ K⁻¹ in the parallel and perpendicular directions, respectively. In both cases, no obvious trend with varying the Te content is observed, to within experimental uncertainty, suggesting that the presence of Te has virtually no influence on the phonon transport due to the low substitution levels achieved. Near 700 K, κ_L approaches the minimum thermal conductivity $\kappa_{min} \approx 0.3$ W m⁻¹ K⁻¹ which represents the lower bound for the lattice thermal conductivity. κ_{min} has been calculated from the transverse and longitudinal sound velocities determined by room-temperature ultrasonic measurements on Pb₅Bi₆Se₁₄ (Refs. 25 and 28) following the model of Cahill and Pohl.³⁷

Dimensionless thermoelectric figure of merit ZT

The temperature dependence of the ZT values is presented in Figure 8a. The peak ZT value of 0.5 at 723 K is nearly independent of the Te concentration due to the increase in κ_e that compensates the increase in the power factor α^2/ρ . The dependence of the experimental ZT values measured at 300, 500 and 700 K on the carrier concentration has been compared to the theoretical curve predicted by the SPB model (Figure 8b). This curve was calculated using the following expressions³⁶

$$ZT = \frac{\alpha^2}{L + (\psi\beta)^{-1}} \quad (5)$$

$$\beta = \frac{\mu_0(m^*/m_e)^{3/2}T^{5/2}}{\kappa_L} \quad (6)$$

$$\psi = 2e \left(\frac{2\pi k_B m_e}{h^2} \right)^{3/2} \frac{F_\lambda(\eta)}{\Gamma(1 + \lambda)} \quad (7)$$

where μ_0 is the intrinsic electron mobility and $\Gamma(x)$ is the gamma function. μ_0 was determined from the Hall mobility μ_H ³⁶

$$\mu_H = \mu_0 \frac{\sqrt{\pi}F_\lambda(\eta)}{2\Gamma(1 + \lambda)F_{1/2}(\eta)} \quad (8)$$

while the κ_L values measured at 300, 500 and 700 K were used and considered constant across the Te concentration range. The less good agreement between the theoretical curve and the experimental data at 700 K compared to 300 and 500 K is due to minority carrier effects that appear above 600 K, the influence of which is not taken into account in the SPB model. This analysis shows that Te-substituted samples exhibit nearly optimal electronic properties without the need for further adjustment of the electron concentration. However, although the SPB model predicts an optimum electron concentration of $2.5 \times 10^{19} \text{ cm}^{-3}$ at 700 K which is close to that achieved experimentally, further optimization of ZT might be possible by considering non-parabolic effects. If significant deviations from parabolic behaviour occur in more heavily-doped samples, probing deeper into the conduction bands would then help to achieve higher thermopower values than in the parabolic case. Although time-consuming for such complex crystal structures, electronic band structure calculations would be helpful in confirming or invalidating this assumption.

Conclusion

In this study, the series $\text{Pb}_5\text{Bi}_6\text{Se}_{14-x}\text{Te}_x$ was successfully synthesized by a two-step synthesis approach. The insertion of Te into the crystal structure was confirmed by a combination of PXRD, SEM and EPMA analyses. The transport properties, investigated in a wide temperature range, showed that increasing x reinforces the metallic character of the transport, as commonly observed in chalcogenides. The very low lattice thermal conductivity inherent to the homologous series $(\text{PbSe})_5(\text{Bi}_2\text{Se}_3)_{3m}$ ($m = 1, 2$ and 3) is only weakly affected by this substitution suggesting no enhancement in point-defect scattering. The beneficial influence of Te on the power factor is counterbalanced by the concomitant increase in the electronic thermal conductivity which leads to similar ZT values of 0.5 at 723 K across this series. Despite the likely non-trivial electronic band structure of these compounds, a single-parabolic band model predicts well the evolution of the electronic properties with x in the concentration range covered. The electron concentration dependence of the ZT values suggests that further enhancement in the thermoelectric performances of this compound might be obtained at higher doping levels where possible non-parabolic band behaviour might emerge. The simplicity of the synthetic method used to synthesize substituted samples of $\text{Pb}_5\text{Bi}_6\text{Se}_{14}$ opens interesting possibilities to control its transport properties given the large number of elements known to dope the two precursors PbSe and Bi_2Se_3 . Beyond thermoelectric properties, extending this approach to the $m = 2$ compound may help to identify adequate dopants for inducing superconductivity in this topological insulator.

References

- 1 *Thermoelectrics and its Energy Harvesting*, ed. D. M. Rowe, CRC Press, 2012.
- 2 H. J. Goldsmid, in *Thermoelectric Refrigeration*, Temple Press Books, Ltd., London, 1964.
- 3 G. Tan, L.-D. Zhao, M. G. Kanatzidis, *Chem. Rev.*, 2016, **116**, 12123–12149.
- 4 A. Mroczek, M. G. Kanatzidis, *Acc. Chem. Res.*, 2003, **36**, 111–119.
- 5 M. G. Kanatzidis, *Acc. Chem. Res.*, 2005, **38**, 359–368.
- 6 B. Makovicky, W. C. Mumme, J. A. Watts, *Can. Mineral.*, 1977, **15**, 339–348.
- 7 A. Pring, M. Jercher, E. Makovicky, *Mineral. Mag.*, 1999, **63**, 917–926.
- 8 A. Olvera, G. Shi, H. Djieutedjeu, A. Page, C. Uher, E. Kioupakis, P. F. P. Poudeu, *Inorg. Chem.*, 2015, **54**, 746–755.
- 9 J. Casamento, J. S. Lopez, N. A. Moroz, A. Olvera, H. Djieutedjeu, A. Page, C. Uher, P. F. P. Poudeu, *Inorg. Chem.*, 2017, **56**, 261–268.
- 10 A. R. Graham, R. M. Thompson, L. G. Berry, *Am. Mineral.*, **1953**, 38, 536–544.
- 11 E. Matzat, *Acta Cryst.*, **1979**, B35, 133–136.
- 12 G. Ferraris, E. Makovicky, S. Merlino, in *Crystallography of Modular Materials*, Oxford Scholarship, 2008.
- 13 E. Makovicky, B. G. Hyde, *Struct. Bonding*, **1981**, 46, 101–170.
- 14 E. Makovicky, B. G. Hyde, in *Incommensurate misfit sandwiched layered compounds*, Ed. A. Meerschaut, Materials Science Forum, vol. 100-101, pp. 1-100, 1992.
- 15 D. Topa, E. Makovicky, H. Dittrich, *Can. Mineral.*, **2010**, 48, 483–495.
- 16 S. V. Borisov, N. V. Pervukhina, S. A. Magarill, N. V. Kuratieva, I. A. Bryzgalov, N. N. Mozgova, I. V. Chaplygin, *Can. Mineral.*, **2012**, 50, 387–395.
- 17 K. Nakayama, K. Eto, Y. Tanaka, T. Sato, S. Souma, T. Takahashi, K. Segawa, Y. Ando, *Phys. Rev. Lett.*, 2012, **109**, 236804.

- 18 S. Sasaki, K. Segawa, Y. Ando, *Phys. Rev. B*, 2014, **90**, 220504(R).
- 19 L. Fang, C. C. Stoumpos, Y. Jia, A. Glatz, D. Y. Chung, H. Claus, U. Welp, W.-K. Kwok, M. G. Kanatzidis, *Phys. Rev. B*, 2014, **90**, 020504(R).
- 20 X. Ren, A. K. Singh, L. Fang, M. G. Kanatzidis, F. Tavazza, A. V. Davydov, L. J. Lauhon, *Nano Lett.*, 2016, **16**, 6064–6069.
- 21 Y. Zhang, A. P. Wilkinson, P. L. Lee, S. D. Shastri, D. Shu, D.-Y. Chung, M. G. Kanatzidis, *J. Appl. Cryst.*, 2005, **38**, 433–441.
- 22 L. Shelimova, O. Karpinskii, P. Konstantinov, E. Avilov, M. Kretova, G. Lubman, I. Y. Nikhezina, V. Zemskov, *Inorg. Mater.*, 2010, **46**, 120–126.
- 23 L. Shelimova, O. Karpinskii, V. Zemskov, *Inorg. Mater.*, 2008, **44**, 927–931.
- 24 V. Zemskov, L. Shelimova, P. Konstantinov, E. Avilov, M. Kretova, I. Y. Nikhezina, *Inorg Mater: Applied Res.*, 2011, **2**, 405–413.
- 25 M. Ohta, D. Y. Chung, M. Kunii, M. G. Kanatzidis, *J. Mater. Chem. A*, 2014, **2**, 20048–20058.
- 26 S. Sassi, C. Candolfi, V. Ohorodniichuk, C. Gendarme, P. Masschelein, A. Dauscher, B. Lenoir, *J. Electron. Mater.*, 2017, **46**, 2790–2796.
- 27 K. Segawa, A. A. Taskin, Y. Ando, *J. Solid State Chem.*, 2015, **221**, 196–201.
- 28 S. Sassi, C. Candolfi, G. Delaizir, S. Migot, J. Ghanbaja, C. Gendarme, A. Dauscher, B. Malaman, B. Lenoir, *Inorg. Chem.* (2017). DOI: 10.1021/acs.inorgchem.7b02656.
- 29 Q. Tan, L.-D. Zhao, J.-F. Li, C.-F. Wu, T.-R. Wei, Z.-B. Xing, M. G. Kanatzidis, *J. Mater. Chem. A*, 2014, **2**, 17302–17306.
- 30 S. Sassi, C. Candolfi, J.-B. Vaney, V. Ohorodniichuk, P. Masschelein, A. Dauscher, B. Lenoir, *Appl. Phys. Lett.*, 2014, **104**, 212105.
- 31 R. Moshwan, L. Yang, J. Zou, Z.-G. Chen, *Adv. Funct. Mater.*, 2017, 1703278.
- 32 G. Dennler, R. Chmielowski, S. Jacob, F. Capet, P. Roussel, S. Zastrow, K. Nielsch, I.

Opahle, G. K. H. Madsen, *Adv. Energy Mater.*, 2014, 1301581.

33 Y. C. Akgöz, G. A. Saunders, *J. Phys. C: Solid State Phys.*, 1975, **8**, 1387–1396.

34 E. Alleno, D. Bérardan, C. Byl, C. Candolfi, R. Daou, R. Decourt, E. Guilmeau, S. Hébert, J. Hejtmanek, B. Lenoir, P. Masschelein, V. Ohorodniichuk, M. Pollet, S. Populoh, D. Ravot, O. Rouleau, M. Soulier, *Rev. Sci. Instrum.*, 2015, **86**, 011301.

35 H. J. Goldsmid, J. W. Sharp, *J. Electron. Mater.*, 1999, **28**, 869–872.

36 V. I. Fistul, *Heavily Doped Semiconductors*, Plenum Press, New York, 1969.

37 D. G. Cahill, S. K. Watson, R. O. Pohl, *Phys. Rev. B*, 1992, **46**, 6131–6140.

Table Captions

Table 1. Nominal and actual compositions measured by EPMA for the $\text{Pb}_5\text{Bi}_6\text{Se}_{14-x}\text{Te}_x$ samples. All the chemical formulas were normalized to 25 atoms per formula unit.

| <i>Nominal composition</i> | <i>EPMA composition</i> |
|---|---|
| $\text{Pb}_5\text{Bi}_6\text{Se}_{14}$ | $\text{Pb}_{4.88\pm 0.05}\text{Bi}_{6.10\pm 0.07}\text{Se}_{14.02\pm 0.07}$ |
| $\text{Pb}_5\text{Bi}_6\text{Se}_{13.75}\text{Te}_{0.25}$ | $\text{Pb}_{5.01\pm 0.20}\text{Bi}_{5.91\pm 0.17}\text{Se}_{13.88\pm 0.07}\text{Te}_{0.20\pm 0.08}$ |
| $\text{Pb}_5\text{Bi}_6\text{Se}_{13.5}\text{Te}_{0.5}$ | $\text{Pb}_{5.00\pm 0.06}\text{Bi}_{5.92\pm 0.05}\text{Se}_{13.64\pm 0.07}\text{Te}_{0.44\pm 0.10}$ |
| $\text{Pb}_5\text{Bi}_6\text{Se}_{13}\text{Te}_1$ | $\text{Pb}_{5.31\pm 0.96}\text{Bi}_{5.67\pm 0.74}\text{Se}_{13.07\pm 0.47}\text{Te}_{0.95\pm 0.45}$ |

Figure Captions

Figure 1. Crystal structure of $\text{Pb}_5\text{Bi}_6\text{Se}_{14}$ (space group $P2_1/m$; $a = 15.959(3)$ Å; $b = 4.1939(9)$ Å; $c = 21.530(5)$ Å; $\beta = 97.39(1)^\circ$ at 300 K) consisting in alternating Pb-Se (blue polyhedra) and Bi-Se (violet polyhedra) layers projected along the b and c axis. The Pb, Bi and Se atoms are shown in blue, violet and dark grey, respectively. In both panels, the monoclinic unit cell is shown by the blue solid lines. In this figure, the five, six and fourteen inequivalent sites for the Pb, Bi and Se atoms, respectively, are not distinguished.

Figure 2. PXRD patterns of the $\text{Pb}_5\text{Bi}_6\text{Se}_{14-x}\text{Te}_x$ samples for $x = 0.0, 0.20, 0.44$ and 0.95 . The main reflections observed for the $x = 0.0$ parent compound are indexed. These patterns are compared to the theoretical pattern determined from single-crystal X-ray diffraction data.

Figure 3. Backscattered electron (BSE) image and corresponding elemental X-ray maps of the illustrative $x = 0.20$ sample (see Figures S1 and S2 in the ESI file for the $x = 0.44$ and 0.95 samples).

Figure 4. Temperature dependence of the (a) electrical resistivity ρ and (b) thermopower α for the $\text{Pb}_5\text{Bi}_6\text{Se}_{14-x}\text{Te}_x$ series measured parallel (filled symbols) and perpendicular (open symbols) to the pressing direction. The color-coded symbols are similar in both panels. The solid lines are guides to the eye.

Figure 5. Temperature dependences of (a) the electron concentration n and (b) Hall mobility μ_H inferred from Hall coefficients measured perpendicular to the pressing direction. The color-coded symbols are similar in both panels. The solid lines are guides to the eye.

Figure 6. Experimental thermopower values α (in absolute values) measured at 300 (red filled circles) and 500 K (blue filled squares) as a function of the room-temperature electron concentration n . The error bars correspond to the experimental uncertainty in the thermopower measurements estimated to be 5%. The solid black lines correspond to the Ioffe-Pisarenko curve calculated using a single-parabolic-band model with a density-of-states effective mass m^* of $0.52 m_e$.

Figure 7. (a) Total thermal conductivity κ as a function of temperature for the series $\text{Pb}_5\text{Bi}_6\text{Se}_{14-x}\text{Te}_x$ measured parallel (filled symbols) and perpendicular (open symbols) to the pressing direction. The data between 200 and 300 K have been discarded due to thermal radiations that are superimposed to the intrinsic κ values in this temperature range. (b) Lattice thermal conductivity κ_L as a function of temperature for samples measured parallel (filled symbols) and perpendicular (open symbols) to the pressing direction. κ_L has been estimated using degeneracy-adjusted Lorenz numbers. The horizontal solid black line stands for the glassy limit. In both panels, the solid lines are guides to the eye.

Figure 8. (a) Temperature dependence of the dimensionless thermoelectric figure of merit ZT for the $\text{Pb}_5\text{Bi}_6\text{Se}_{14-x}\text{Te}_x$ samples measured parallel (filled symbols) and perpendicular (open symbols) to the pressing direction. The solid lines are guides to the eye. (b) Experimental ZT values measured at 300, 500 and 700 K as a function of the electron concentration. The error bars correspond to the experimental uncertainty estimated to be 17%. The solid black lines were calculated using the SPB model with a constant density-of-states effective mass m^* of $0.52 m_e$, intrinsic mobilities μ_0 of 20, 16 and 12 $\text{cm}^2 \text{V}^{-1} \text{s}^{-1}$ and lattice thermal conductivities κ_L of 0.60, 0.44 and 0.34 $\text{W m}^{-1} \text{K}^{-1}$ at 300, 500 and 700 K, respectively.

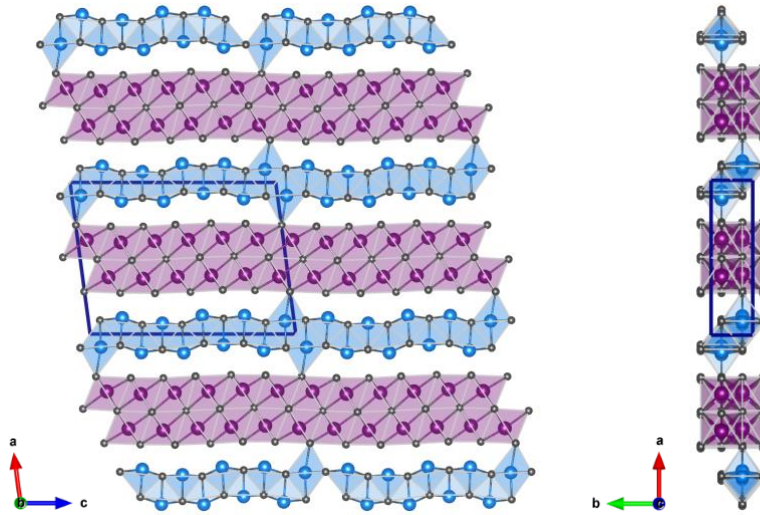


Figure 1

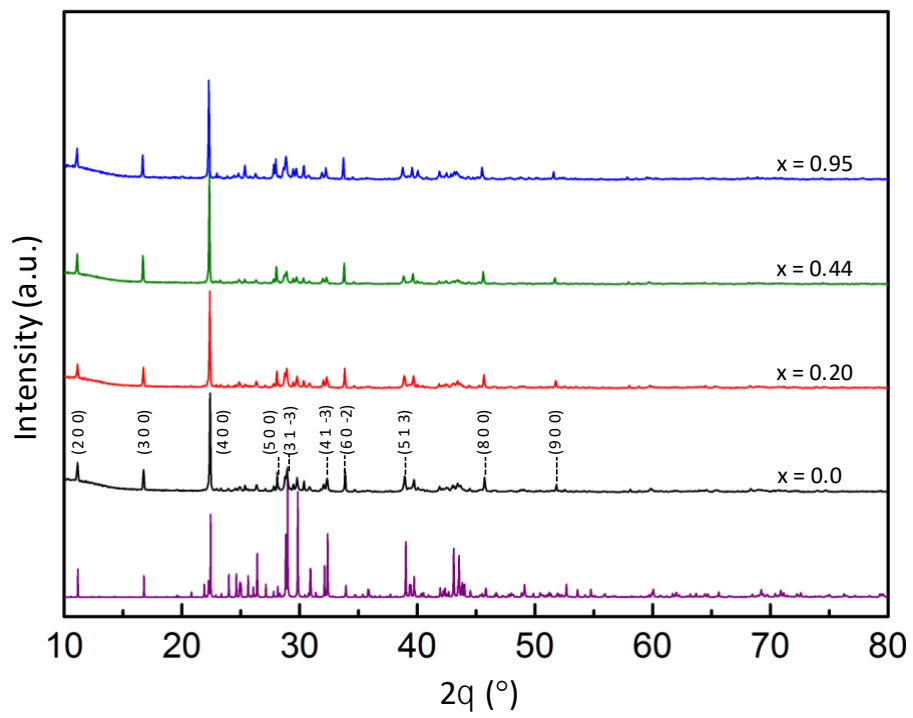


Figure 2

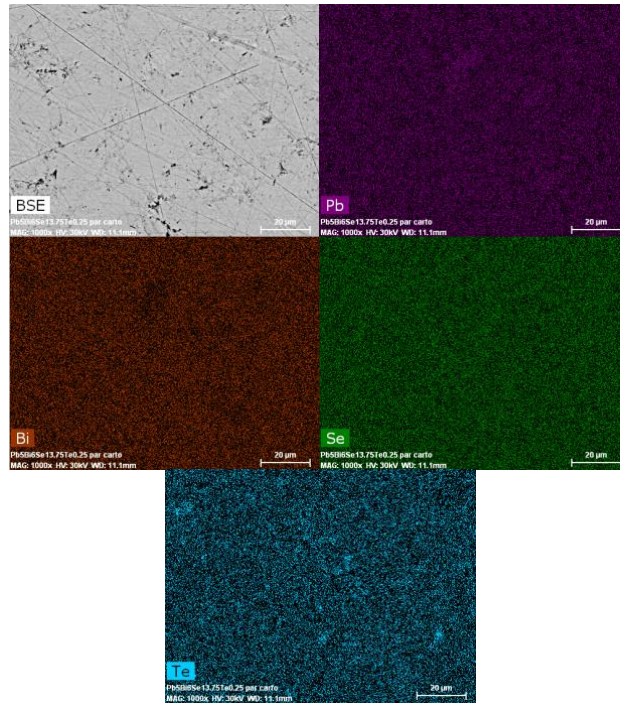


Figure 3

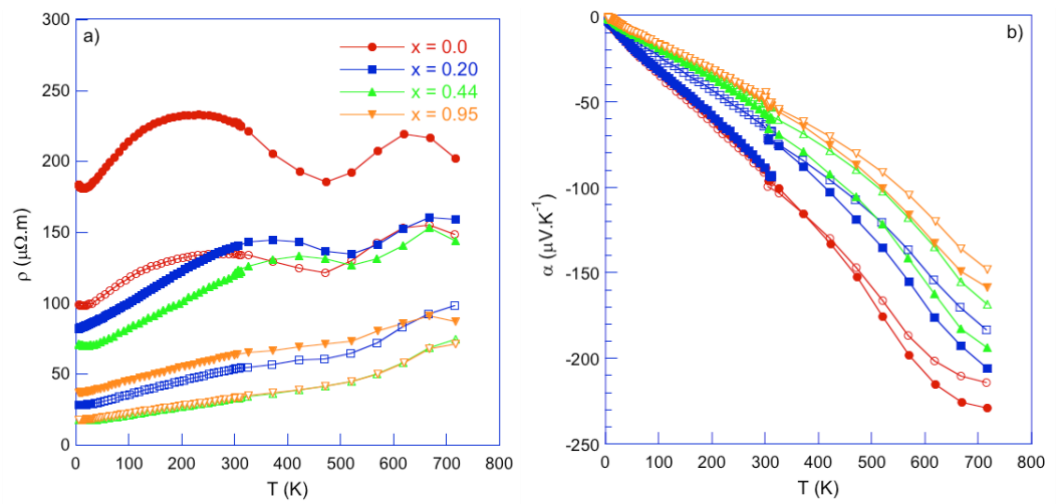


Figure 4

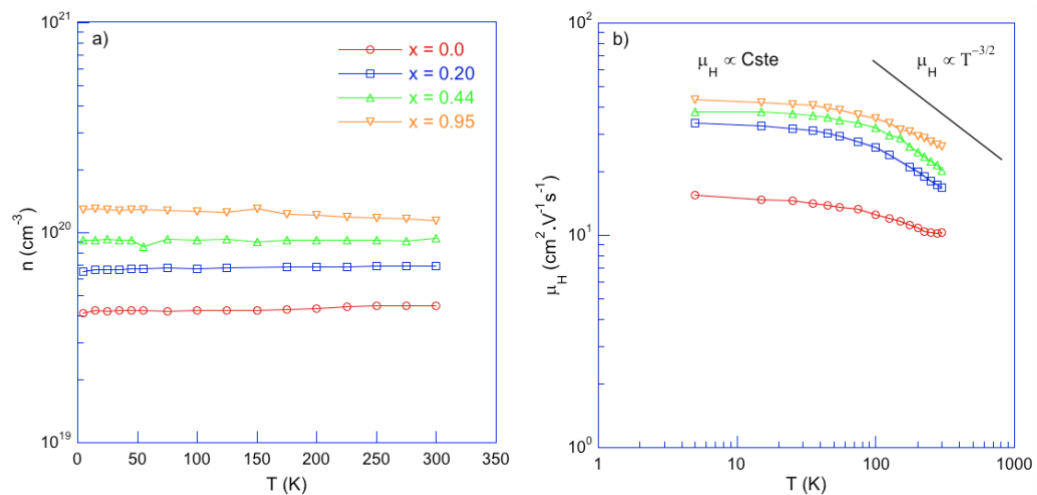


Figure 5

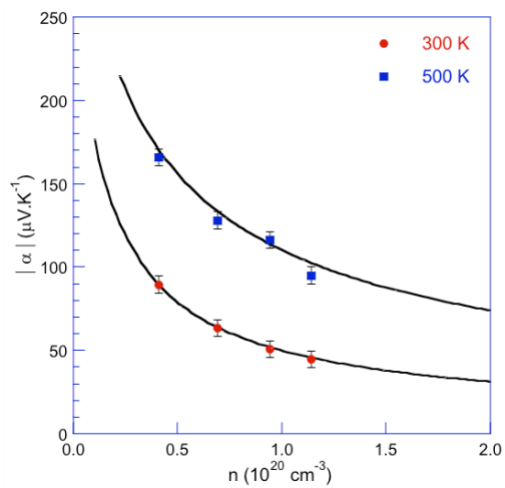


Figure 6

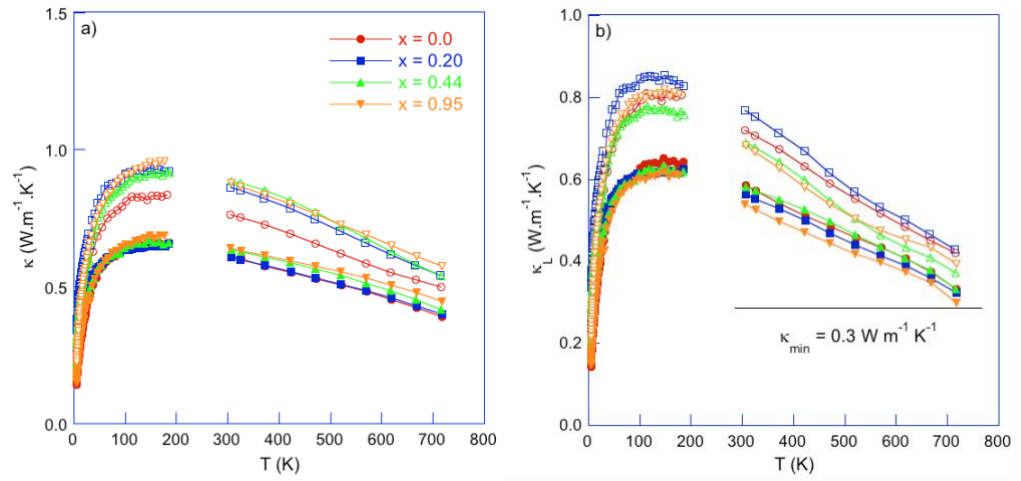


Figure 7

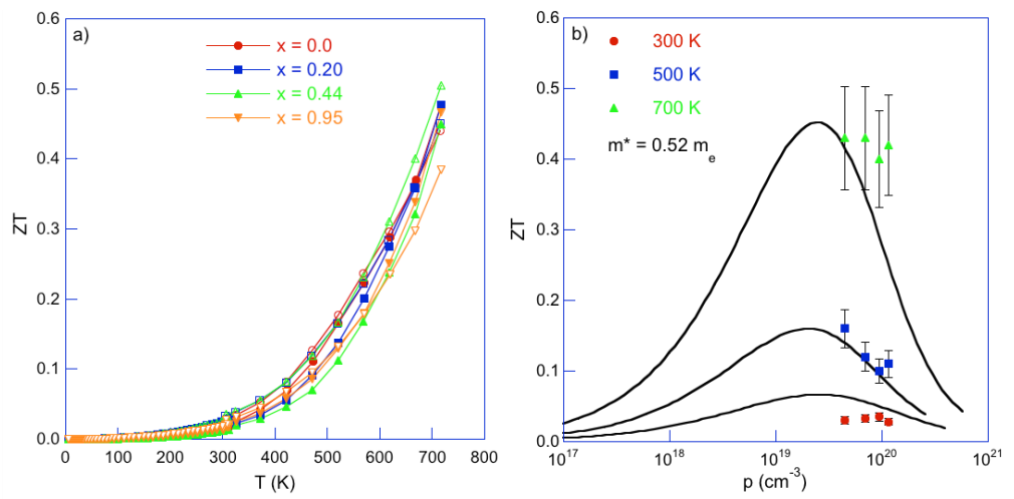


Figure 8